Final Report

NASA Innovative Advanced Concepts (NIAC)
Phase I

StarNAV: An Architecture for Autonomous Spacecraft Navigation by the Relativistic Perturbation of Starlight

Award#: 80NSSC20K1018

John A. Christian (PI)
Paul McKee (Graduate Student)
Rensselaer Polytechnic Institute

Michael Kudenov (Co-I)
Hoang Nguyen (Graduate Student)
North Carolina State University

May 2021

Rensselaer Polytechnic Institute
110 8th Street
Troy, NY 12180

Table of Contents

1 Introduction

Exploration missions to the outer Solar System (e.g., Neptune, Kuiper belt objects) or to the interstellar medium present several challenges for conventional spacecraft designs. One of the greatest challenges is a means for navigation, as Earth-based tracking with the Deep Space Network (DSN) becomes less desirable due to high cost, decreased performance at long ranges, and long light-time delays. Indeed, light time delays at Neptune are over four hours (one way), making control of spacecraft during critical events nearly impossible—and this problem only becomes worse as we move to the Kuiper belt or to interstellar space.

The need for autonomous spacecraft navigation is well established and is prominently featured in the 2015 NASA Technology Roadmap (e.g., TA 5.4.2.6 & 5.4.2.8). This has led to investment in various technologies to accomplish this task, with the majority of recent work focusing on optical navigation (OPNAV; TA 5.4.4.1) [1], X-ray pulsar navigation (XNAV; TA 5.6.1) [2], or DSN one-way ranging with the Deep Space Atomic Clock (DSAC; TA 5.4.1.1) [3]. **This NIAC study suggests a new (and completely different) way of autonomously navigating a spacecraft anywhere in the Solar System or beyond. We call this new technique StarNAV.**

1.1 The StarNAV Concept

StarNAV uses the relativistic perturbation of starlight to infer spacecraft velocity [4], which may be used for navigation [5]. Compared to an observer at rest, a sensor aboard a spacecraft will observe light from a star at a slightly different direction (stellar aberration) and at a slightly different wavelength (relativistic Doppler effect). Preliminary work in this area [4] suggests that velocity estimation by observing the Doppler shift of stellar spectra is exceedingly difficult (due to short-term instability of stellar spectra and instrument calibration challenges)—a finding in agreement with earlier considerations of navigation by Doppler shift [6]. In contrast, velocity estimation by stellar aberration requires bearing measurements with errors at the milliarcsecond level, which is well within the capability of modern astrometric instruments.

The conventional use of stars in spacecraft navigation is exclusively for attitude determination. Even when stars are used within the context of OPNAV (e.g., star-horizon measurements) the function of the star observations is to provide a reference direction in inertial space, not to provide information on the translational state (this comes from observations of the "nearby" celestial body). In all cases, precision navigation with stars requires an estimate of velocity be provided to remove the effect of stellar aberration [7]. The effect of stellar aberration can produce attitude errors on the order of 26 arcseconds in low Earth orbit (LEO). **In StarNAV, we transform stellar aberration—which is generally considered a nuisance parameter—into the navigation observable. This represents a fundamental change in how stars are used for navigation.**

Absolute star bearing measurements at the milliarcsecond level are difficult to achieve in real-time due to limitations in vehicle-level attitude determination and control. Therefore, the StarNAV technique only considers inter-star angles, which entirely removes the need for attitude estimation in construction of the StarNAV solution (although excellent attitude knowledge is still needed to point the StarNAV instrument). Preliminary results suggest that inter-star angles can be measured with both the requisite accuracy and precision [4].

1.2 Major Accomplishments during NIAC Phase I Study

During the course of this NIAC Phase I study, we investigated three main topics. These are briefly summarized below. These tasks are in general agreement with the originally proposed tasks, with a few minor modifications that arose as a result of the research. A detailed accounting of the results associated with each accomplishment is provided in the Technical Results section of this report.

1. Star identification: StarNAV requires us to match star observations to corresponding known stars from a catalog. This necessitates solving the star identification problem. We explored conventional star ID techniques within the context of StarNAV, finding these legacy techniques to be suitable for some mission scenarios and unsuitable for others.

2. StarNAV sensor configurations: The original StarNAV sensor concept consisted of the accurate measurement of the angle between a pair of stars—achieved using a system of telescopes and/or interferometers. In addition to this, we explored the efficacy of StarNAV with a wide field-of-view sensor that simultaneously processes a very large number of stars. A detailed feasibility of the wide FOV concept was performed.

3. StarNAV for interstellar missions: Unlike many conventional navigation techniques, StarNAV remains available anywhere in the Solar System and into interstellar space. This makes StarNAV an interesting technology to consider within the context of missions currently in development to explore the interstellar medium. Challenges remain for star identification and some examples are shown to highlight some of the important issues.

2 Technical Results

2.1 Star Identification

Portions of this section also appear in Refs. [8] and [9], which were completed with funding from this NIAC Phase I grant. The mathematical details are only summarized here and the interested reader is directed to these references details.

There are a variety of situations where it is necessary to autonomously recognize an asterism (i.e., a star pattern). This occurs when using a StarNAV system, when solving the lost-in-space attitude determination problem with star trackers, when registering scientific astronomical images, and in other applications. Thus, while motivated by StarNAV in this context, advances in star identification have wide-reaching benefits to the space exploration community. The discussion that follows assumes the stars are seen in an image, such as with a telescope, star tracker, camera, or the StarNAV sensor concept in Section 2.2.2.

For an asterism to be recognizable in a single image, there must be some attribute of the pattern that is always recoverable from only its appearance in the image. This attribute could be related to geometric or photometric properties of the asterism. While could be used, difficulty with accurately measuring the photometric properties of stars with low-cost sensors make it desirable to recognize asterisms with the pattern geometry alone. The usual approach is to find some descriptive attributes of the pattern that are *invariant* to attitude (and, perhaps, camera calibration) so that they may be computed ahead of time and stored in an onboard catalog. Then, when an image is collected aboard a spacecraft at an unknown attitude (and, perhaps, with an

unknown calibration), these descriptive asterism attributes may be computed from the image and directly compared against the precomputed catalog.

There have been a great variety of asterism descriptors proposed over the years. These descriptors, however, are not as different from one another as they may first seem. Moreover, in many cases, the different descriptors solve slightly different pattern recognition problems—often without a clear discussion of this important fact. Therefore, following the philosophical approach of Refs. [10] and [11] this work provides a theoretical framework for developing invariant descriptors for asterisms as seen in an image from a projective camera. Popular existing asterism descriptors used for star identification are shown to be example cases within this framework.

Analysis of the geometry reveals that there are (at least) four fundamental classes of optical system for which invariant asterism descriptors may be built: generic calibrated camera, narrow field-of-view (FOV) calibrated camera, generic uncalibrated camera, narrow FOV uncalibrated camera. Good descriptor options already exist for some of these cases and we developed novel descriptors for others.

Invariant asterism descriptors are the mathematical construct around which practical star identification algorithms are built. To match an observed descriptor to its corresponding catalog entry requires us to consider the interplay between (1) the stability of these descriptors in the presence of measurement noise, (2) the makeup of the full star catalog along with a scheme for choosing which star asterisms to index, and (3) the data structure used to mechanize the real-time index search on a digital computer. A specific star identification algorithm represents a specific choice for each of these three tasks. Numerical simulations and live-sky experiments between different algorithms are important here, though simple changes to any choice in the pipeline can significantly affect overall performance—often making a fair comparison between competing algorithms difficult. Numerical comparisons of some existing algorithms may be found elsewhere [12,13]. Our contribution here is not the development of new star identification algorithms, but a better theoretical framework for understanding how the vast majority of these algorithms actually function. Such a framework provides a valuable tool for spacecraft navigators that seek a more mathematically rigorous (as opposed to a heuristic) approach for developing and evaluating star identification algorithms.

2.1.1 Asterism Descriptors Inside our Solar Systems

To recognize an asterism (i.e., star pattern) using only the pixel coordinates of the stars in an image, we require a means of describing the pattern geometry that remains unchanged under the action of a projective camera at unknown attitude. This is achieved by computing algebraic quantities that are (1) functions of only the observed star coordinates, (2) invariant under changes in camera attitude, and (3) have different numerical values for each asterism. The collection of these algebraic quantities (referred to here simply as *invariants*) may be used to construct asterism descriptors. The proper mathematical framework for addressing this problem is invariant theory [14].

Constructing invariants requires the consideration of both the algebraic variety and the group acting on that algebraic variety. We observed that algebraic variety describing a star direction is simply a point in $\mathbb{P}^2$. For more on the properties of n-dimensional projective space ($\mathbb{P}^n$), the reader

is referred to Refs. [1] and [15]. Therefore, letting $\mathcal{V}$ be the variety of a d-tuple of star directions, we find that $\mathcal{V} \cong (\mathbb{P}^2)^d$ has dimension $2d$.

Within the Solar System, the location of stars can be well approximated as points on the celestial sphere—or, as discussed above, a point in $\mathbb{P}^2$. In this case, both the star catalog and the star observations are points in $\mathbb{P}^2$, and they are related by the mapping $\pi : \mathbb{P}^2 \to \mathbb{P}^2$. As we will soon see, our ability to robustly recognize star patterns is entirely dependent on the assumption that stars are very far away and can be (approximately) modeled as points $\mathbb{P}^2$.

Different assumptions about the camera give rise to different group actions on $\mathcal{V}$. These different group actions, in turn, give rise to different invariants and different asterism descriptors. A summary of the most commonly encountered scenarios is provided in Table 1.

Table 1. Overview of invariants for asterisms as viewed from within our Solar System. For a full accounting of all the invariants, see Ref. [8].

Camera Type	Group Action	Number of Independent Invariants	Example Invariants
Calibrated Wide FOV	Special Orthogonal Group, SO(3)	$2d$-3	Inter-star Angle, Dihedral Angle
Calibrated Narrow FOV	Euclidian Group, E(2)	$2d$-3	Inter-star Distance
Uncalibrated Wide FOV	Projective General Linear Group, PGL(3)	$2d$-8	Cross-Ratio
Uncalibrated Narrow FOV	Similarity Group, S(2)	$2d$-4	Interior Angles, Canonical Coordinates

2.1.2 Asterism Descriptors Outside our Solar Systems

As a spacecraft moves to an unknown galactic location far away from our Solar System, we find the simplifying condition used in Section 2.1.1 to no longer be true. The result is substantial parallax for a large number of stars that will change the apparent star pattern seen by an observer aboard the interstellar spacecraft. The changing star patterns due to parallax is an important effect to consider.

For a spacecraft at an arbitrary location in the galaxy to recognize an apparent pattern of stars, we must assume stars are 3D points in space with LOS measurements described by the mapping $\pi : \mathbb{P}^3 \to \mathbb{P}^2$. Following the same procedure as before, we might expect that invariants will arise when we consider an asterism of a sufficiently large number of stars. The trouble, however, is that the the algebraic variety $\mathcal{M} \subseteq (\mathbb{P}^2)^d$ formed by $\pi : \mathbb{P}^3 \to \mathbb{P}^2$ does not produce an orbit for any group action on $(\mathbb{P}^2)^d$, as is discussed at length in Ref [16]. As a consequence, we find there are no invariants. That invariants do not exist for the projection of 3D points in general position has been known for some time [16,17,18], and we now present an especially concise proof of this fact within the context of interstellar star identification.

2.1.2.1 Notation

To proceed, we introduce the following compact notation. Let a *d*-tuple of stars modeled as three-dimensional points be given by the algebraic variety $\mathcal{W} \cong (\mathbb{P}^3)^d$, which has dimension $3d$. Then, let $U \in \mathcal{M}$ be the sensor observations from pose V of the specific *d*-tuple of stars $S \in \mathcal{W}$. We write this compactly as

$$U = \pi(S, V) \tag{1}$$

Moreover, the idea behind invariant-based star identification is that there is some algebraic quantity that may be computed from the measurements that is unchanged by (is *invariant* to) changes in the sensor pose. Since the invariant is computed from the measurements, we may write it as $I(U)$ or, more conveniently, as $I(\pi(S, V))$. Since $I(\pi(S, V))$ is unchanged by the sensor pose, it follows that

$$I\big(\pi(S, V_k)\big) = I\big(\pi(S, V_\ell)\big), \qquad \forall\, k, \ell \tag{2}$$

2.1.2.2 The Non-Existence of Projective Invariants for 3D Stars

Now, suppose we have two *d*-tuples of stars S_1 and S_2. Regardless of the sensor's state (galactic position and attitude) or the configuration of stars in S_1 or S_2, we can show that any invariant of S_1 must also be an invariant of S_2—meaning that the only invariants that exist are both trivial and non-unique. This is now shown.

Begin with the *d*-tuple of stars in S_1. Let any given star's 3D coordinates be given by $\boldsymbol{s}_{\{\cdot\}} \in \mathbb{R}^3$. Now, form a new *d*-tuple of stars, $S_1^{(i)}$, where we have exchanged the first *i* stars in S_1 with the first *i* stars in S_2. That is, if we have

$$S_1 = \left\{ \boldsymbol{s}_{1_1}, \boldsymbol{s}_{1_2}, \boldsymbol{s}_{1_3}, \dots, \boldsymbol{s}_{1_d} \right\} \tag{3}$$
$$S_2 = \left\{ \boldsymbol{s}_{2_1}, \boldsymbol{s}_{2_2}, \boldsymbol{s}_{2_3}, \dots, \boldsymbol{s}_{2_d} \right\} \tag{4}$$

then we define

$$S_1^{(i)} = \left\{ \boldsymbol{s}_{2_1}, \dots, \boldsymbol{s}_{2_i}, \boldsymbol{s}_{1_{i+1}}, \dots, \boldsymbol{s}_{1_d} \right\} \tag{5}$$

It follows, therefore, that $S_1^{\{(d)\}} = S_2$.

Now, let us proceed by considering the star sets S_1 and $S_1^{(1)}$. Given these two point sets, suppose we have a sensor located at a position somewhere along the 3D line that passes through the 3D points $\boldsymbol{s}_{1_1}$ and $\boldsymbol{s}_{2_1}$ (which happen to be the only two points that are different between the star sets S_1 and $S_1^{(1)}$). As shown in Figure 1, we find that any sensor position V_1 along this line produces a common observation set U_1 for both S_1 and $S_1^{(1)}$:

$$U_1 = \pi(S_1, V_1) = \pi\left(S_1^{(1)}, V_1\right) \tag{6}$$

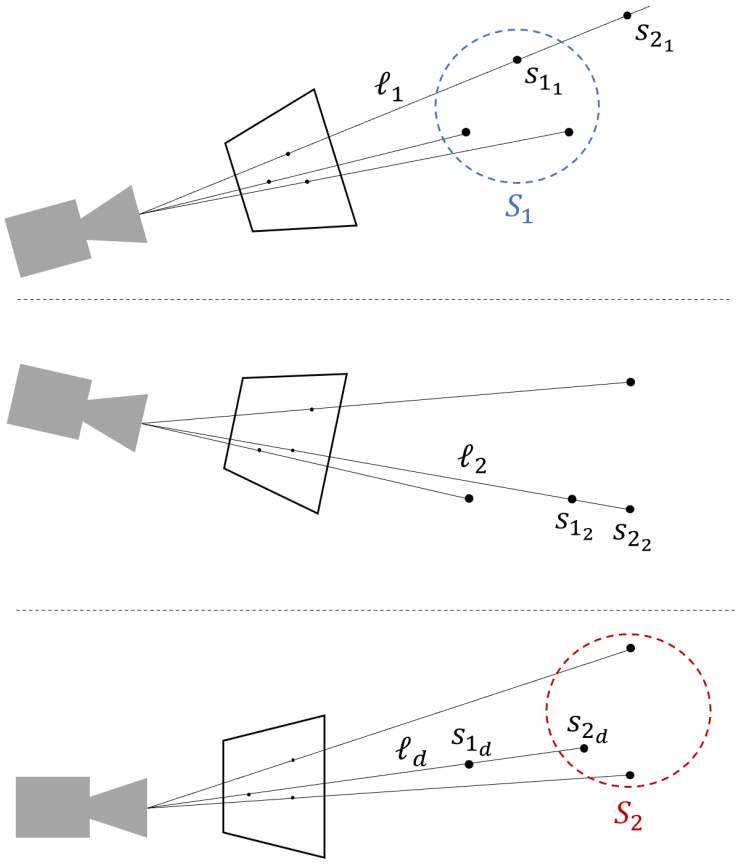

Figure 1. Illustration of invariant chain between two 3D point sets. Top: Point sets S_1 and $S_1^{\{(1)\}}$ with all but one point in common will project to the same image for any pose along line ℓ_1 defined by s_{1_1} and s_{2_1}. Middle: Two point sets $S_1^{(1)}$ and $S_1^{(2)}$ with all but one point in common will project to the same image for any pose along line ℓ_2 defined by s_{2_1} and s_{2_2}. Bottom: Two point sets $S_1^{(d-1)}$ and $S_1^{(d)} = S_2$ with with all but one point in common will project to the same image for any pose along line ℓ_d defined by s_{1_d} and s_{2_d}.

We may now compute invariants from the point set U_1,

$$I(U_1) \;=\; I\big(\,\pi(S_1, V_1)\big) \;=\; I\left(\,\pi\left(S_1^{(1)}, V_1\right)\right) \tag{7}$$

Applying the fact that invariants must remain constant from different poses [see Eq. (2)], the invariants from Eq. (7) become

$$I\big(\,\pi(S_1, V_k)\big) \;=\; I\big(\,\pi(S_1, V_1)\big) \;=\; I\left(\,\pi\left(S_1^{(1)}, V_1\right)\right) \;=\; I\left(\,\pi\left(S_1^{(1)}, V_\ell\right)\right) \tag{7}$$

It follows, therefore, that any invariants for S_1 from arbitrary pose V_k must always be the same as the invariants for $S_1^{(1)}$ from some other arbitrary pose V_ℓ. By removing the middle two terms in Eq. (7) we may write this compactly as

$$I\left(\pi(S_1, V_k)\right) = I\left(\pi\left(S_1^{(1)}, V_\ell\right)\right) \tag{8}$$

Consider now the star sets $S_1^{(1)}$ and $S_1^{(2)}$. Following the same scheme as before, construct the 3D line passing through the 3D points $\boldsymbol{s}_{1_2}$ and s_{2_2} (which happen to be the only two points that are different between the star sets $S_1^{(1)}$ and $S_1^{(2)}$). Placing the pose V_2 somewhere along this line, we produce the observation set U_2

$$U_2 = \pi\left(S_1^{(1)}, V_2\right) = \pi\left(S_1^{(2)}, V_2\right) \tag{9}$$

As before, we find that

$$I\left(\pi\left(S_1^{(1)}, V_\ell\right)\right) = I\left(\pi\left(S_1^{(1)}, V_2\right)\right) = I\left(\pi\left(S_1^{(2)}, V_2\right)\right) = I\left(\pi\left(S_1^{(2)}, V_m\right)\right) \tag{10}$$

for any pose V_ℓ and V_m. Combining this result with Eq. (8), we find that

$$I\left(\pi(S_1, V_k)\right) = I\left(\pi\left(S_1^{(1)}, V_\ell\right)\right) = I\left(\pi\left(S_1^{(2)}, V_m\right)\right) \tag{11}$$

for any three poses V_k, V_ℓ, and V_m.

This procedure is repeated d times until we reach $S_1^{(d)} = S_2$. The end result is that

$$I\left(\pi(S_1, V_k)\right) = I\left(\pi\left(S_1^{(1)}, V_\ell\right)\right) = \cdots = I\left(\pi\left(S_1^{(d)}, V_m\right)\right) = I\left(\pi(S_2, V_n)\right) \tag{12}$$

for any poses V_k, V_ℓ, V_m, and V_n. Writing the final result more explicitly,

$$I\left(\pi(S_1, V_k)\right) = I\left(\pi(S_2, V_n)\right) \tag{13}$$

Consequently, we find that any invariants of the arbitrary star set S_1 viewed from the arbitrary pose V_k must be identical to the invariants of the arbitrary star set S_2 viewed from the arbitrary pose V_n. It follows that all d-tuples of stars S_j have the same invariants, hence these invariants cannot be used to distinguish one asterism from another. **Thus, invariant-based star identification is impossible at a completely unknown galactic location using only line-of-sight measurements to stars.** Identification requires some form of additional information, which may come in the form of constraints on the spacecraft state (position or attitude) or additional measurement types. Preliminary work suggests constraining the motion to a line—a good approximation for long periods of time along an interstellar trajectory—will reintroduce invariants to the interstellar star ID problem. This is a topic of future work.

2.1.3 Matching Asterism Descriptors to a Star Catalog

Regardless of the assumed camera type or the specific invariants chosen for that camera type, we obtain a set of numerical values (the invariants) from the observed asterism that must be matched to corresponding values from a star catalog. This type of invariant-based indexing problem is not unique to star identification and occurs widely in other application domains [18,19,20].

The fundamental idea behind invariant-based matching is that catalog asterisms and measured image asterisms are mapped into a common index space where direct comparison is always possible (see Figure 2). For the case of star identification, each star in the catalog space and image space is a point in $\mathbb{P}^2$. Defining G to be the number of independent invariants (e.g., $G = 2d - 3$ for asterisms of d stars as viewed by a calibrated camera; see Table 1), each asterism may be mapped to a single point in $\mathbb{R}^G$. One simple way to describe this point in index space is with a $G \times 1$ vector formed by concatenation of the G independent invariants in a specified order. The vast majority of past star identification algorithms are simply different schemes to find the closest catalog points to a query point (formed by the observed asterism in an image) within the index space, though few of these algorithms make the abstraction to index space explicit.

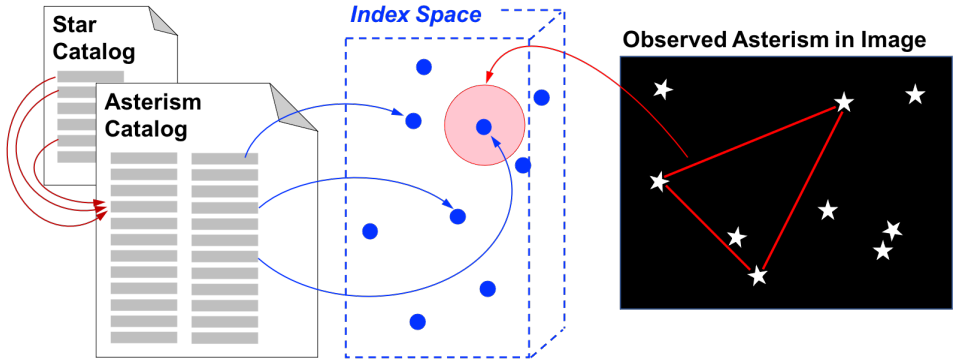

Figure 2. Mapping of entries from a catalog of known star asterisms and from a measured image asterism into a common index space. Measurement noise requires us to search a small region of the index space to find all potential matches from the catalog.

When viewed using the index space abstraction, most successful star identification algorithms have the same overall framework. First, stars are grouped into asterisms (containing two or more stars) and invariants are computed using data from the star catalog and placed into an index. This task is performed offline and infrequently (perhaps only once). Later, an image is captured and the same invariants are computed. These invariants are used to query the index and produce a small list of feasible matches for the observed asterisms. These match hypotheses are then verified using additional information by additional checks.

While the conceptual framework is the same, practical challenges with implementing the above steps lead to a number of different (and equally reasonable) ways of performing robust star identification. The majority of these differences arise from how one chooses to balance the competing priorities of asterism uniqueness, index size, and index query speed. Different choices for the invariants lead to even more variations on this common theme. It should come as no surprise, therefore, that so many different star identification algorithms have been published over the last 50 years [12,13]

Asterisms containing more stars (large d) are more unique. This improving uniqueness occurs since each asterism is a point in index space and more stars increases the dimension of the index space (large $d \rightarrow$ large G). In general (not just for star identification), the number of feasible index matches for any given query decreases exponentially with an increase in G [18]. This would suggest forming asterisms of many stars, since increasing d would increase the likelihood that an observed asterism produces only one feasible match in the index. Moreover, for a sufficiently large G there is no need for subsequent match verification since the likelihood of a false match occurring (i.e., having a randomly occurring nearby point in index space) becomes vanishingly small in a very high dimensional index space.

The direct matching of asterisms containing many stars (large d) is often impractical. For a star catalog containing M stars, the worst case number of asterisms is $\binom{M}{d}$. Since it is always the case that $M \gg d$, the number of asterisms grows exponentially as d increases. Thus, using asterisms of more stars leads to an exponential growth in index size and the problem quickly becomes intractable.

The intractability of catalog size is almost always addressed using a two-part strategy. The first part is to not consider all possible $\binom{M}{d}$ asterisms. Presuming the star identification is to be performed on a digital image from a projective camera, the sensor FOV is limited and there is no need to consider asterisms whose angular extent is larger than the camera FOV. For example, consider two of the most popular contemporary star identification methods: the Pyramid approach [21] and the so-called "Astrometry.net" approach [22]. Pyramid creates an index of inter-star angles corresponding to two-star asterisms, with the index limited to only star pairs whose angular separation is less than a maximum threshold (usually taken as the camera FOV). Astrometry.net uses a similarity transformation to create a four-dimensional descriptor (what they call a ``geometric hash code") corresponding to a four-star asterism (a star quad), with the index limited by tiling the celestial sphere using HEALPix [23]. HEALPix tiles are chosen to be about 1/3 the size of an image and only the brightest stars in each tile are kept. Then a specified number of four-star asterisms smaller than a specified size are generated for each HEALPix tile (using the brightest stars first). In both cases (Pyramid and Astrometry.net) the index building procedure produces substantially fewer than $\binom{M}{d}$ entries. Other star identification pipelines use other approaches, though the end goal managing index size while maintaining good coverage of possible asterisms is essentially the same.

The second part of the usual strategy for dealing with a large asterism index is to query the index using efficient data structures. While the practical constraints of the first part does slow the exponential growth of index size with increasing d, larger asterisms still produce a larger index—oftentimes too large to permit brute force matching. Fast matching to the index is essential since this task is often performed many times before a match is verified. If an image contains N observed stars, there are $\binom{N}{d}$ asterisms that can be built from these stars. With $d!$ permutations of star assignments for each asterism, there are a total of up to $N!/(N-d)!$ possibilities that must be considered. The average time to find a solution can sometimes be improved by not dwelling on certain star observations (which may be false returns or excessively noisy) when checking these combinations and there are a number of deterministic pattern shifting algorithms for doing this [24].

There are a variety of data structures that may be used to accelerate real-time matching, including a *k*-d tree, R-tree, an *n*-d *k*-vector, or others [20,25]. As an example, consider again the popular Pyramid and Astrometry.net pipelines. The original Pryramid approach [21] selects three observed stars and computes the three corresponding inter-star angles. For each inter-star angle, a separate index search is performed using 1-d *k*-vector to find feasible corresponding star pairs from the catalog. The results are combined to see if there is a unique set of star correspondences that amongst the index returns. Thus, Pyramid is an example of a case where searching is done one dimension at a time (rather than all at once). The Astrometry.net approach [22] uses a four-dimensional descriptor which is directly matched with a single query of a four-dimensional *k*-d tree.

The compromise between asterism uniqueness (which is better for a larger *d*) and index size (which is better for a smaller *d*) generally drives solutions star identification pipelines towards the smallest possible *d*. This usually requires match hypotheses be verified since the dimension of *G* is not high enough to keep the likelihood of a false match below an acceptable threshold. The Pyramid approach [21] achieves this verification by checking the three inter-star angles (only two of which are independent) between the three stars forming the triangle match hypothesis and a fourth star—these four stars from the so-called *pyramid* from which this algorithm derives its name. The Astrometry.net approach [22] achieves this verification by using the match hypothesis to compute the attitude, reprojecting catalog stars onto the image, and making additional star correspondences until a Bayes factor metric exceeds a conservative threshold.

2.2 StarNAV Sensor Configuration

2.2.1 Star Pair Sensor

Portions of this section also appear in Ref. [26], which was completed with funding from this NIAC Phase I grant.

2.2.1.1 Error Budget for a Two-Star StarNAV Sensor

In this work, we considered a two-star StarNAV sensor consisting of a roof mirror and parabolic mirror shown in Figure 3. This sensor configuration allows for light from both stars to be focused onto a common focal plane array (FPA), which is advantageous for a sensor calibration.

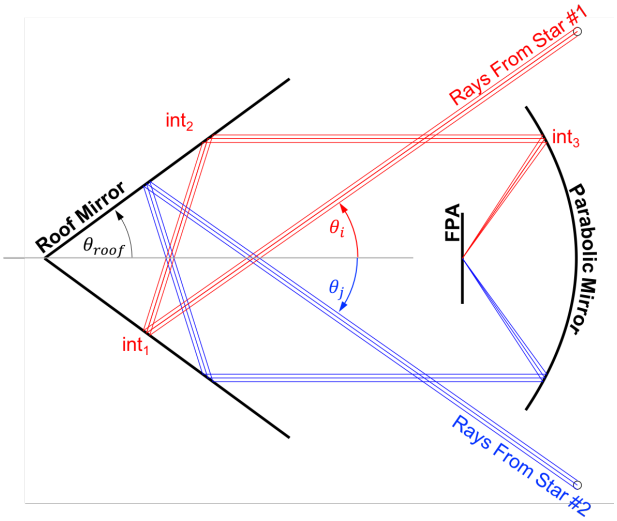

Figure 3. Schematic of example two-star StarNAV system with a roof mirror and parabolic mirror.

Considering the primary error sources, we developed an error budget for such a two-star system necessary to achieve a 1.0 milliarcsec inter-star angle measurement. This error budget is shown in Table 2. Further details regarding the mathematical derivation of the error budget may be found in Ref. [26].

Table 2. Allocated post-calibration error budget for two-star StarNAV sensor.

Component	Allocated Error
Light Baffle	150 μas
Roof Mirror	400 μas
Parabolic Mirror	500 μas
Detector Geometry	200 μas
Vibration	400 μas
Centroiding Algorithm	500 μas
Margin	342 μas
Total (RSS)	1,000 μas (1.0 mas)

2.2.1.2 Waveguide approach for a Two-Star StarNAV Sensor

As an alternative to a straightforward reflective system (e.g., the design in Figure 3) and to improve the precision, we also considered a system utilizing many reflections. One possibility is to extend our two-reflection design by increasing the number of mirrors and offset the reflection angles, thereby folding the optical path. However, each additional element would require calibration and increase costs and complexity. Therefore, our goal is to fold the optical path without adding more mirrors. This can be achieved by an optical waveguide, where a small deviation in incident angle is mapped to a large positional change of the image at the detector.

We model a planar waveguide as two mirrors in parallel. The goal of this model is to show that a sub- milliarcsecond angular sensitivity can be achieved at the detector-side. We assume that the

positional resolution of the detector is 1/10th of a pixel. Therefore, we aim to show in this approach that a 0.1 milliarcsecond change in inter-star angle can yield a positional shift of the image by 1/10th of a pixel or more. For the following calculations, we assume a pixel pitch of 5 μm. A triangle wave function is used to model the nominal ray path within the optical waveguide.

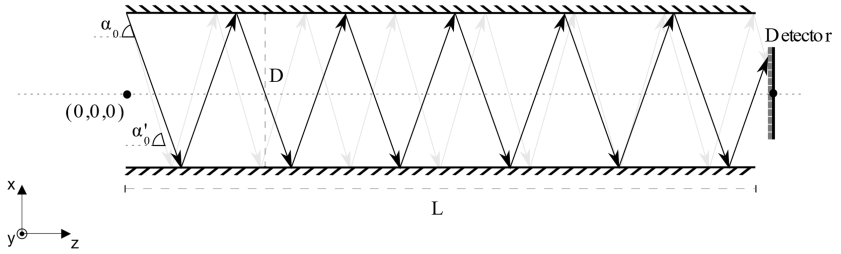

Figure 4. Diagram illustrating optical waveguide approach. Although the incident angles α_0 and α_0' vary by a small degree, due to the large number of reflections, the ray-paths vary greatly.

As a function of the input angle, α_0, distance along the waveguide, z, and distance between the reflective surfaces D, the triangular wave function evaluates to the distance in the x direction.

$$x = Tri(\alpha_0, z, D) = \frac{\mathrm{D}}{2} - \frac{D}{\pi} arccos\left(\cos\left(\frac{z\pi}{D} tan(\alpha_0)\right)\right) \tag{14}$$

and the number of half-periods or reflections (R) is given as:

$$R = \left\lfloor \frac{z\, tan(\alpha_0)}{D} \right\rfloor \tag{15}$$

Taking the partial derivative of Eq. (14) with respect to α_0, where the trigonometric functions are in radians, the angular sensitivity, in length units per radian, is given as:

$$\frac{\partial x}{\partial \alpha_0} = -z\, sec^2(\alpha_0) \tag{16}$$

Notably, the angular sensitivity is independent with respect to D, but proportional to distance along the waveguide. For an angular sensitivity of 0.5 micron per 0.1 milliarcsecond (1.8E3 μm/deg) and a length z = 300 mm, an incident ray angle of 86.91 deg or greater is required. From Eq. (15), for a spacing D = 100 mm, 55 reflections occur in total.

Radiometric Considerations: In waveguides where the principle of optical confinement is through total internal reflection (TIR), complete reflection occurs where the incident angle of light is at or greater than the critical angle. However, because of the angle of the incident light required for a large number of reflections, TIR would be difficult to achieve. Therefore, conventional reflective surfaces are required. For a surface with 99% reflectance, the total power loss after 55 reflections is 42.46%, while 99.9% reflectance yields only 5.35% power loss, assuming a constant reflectance across the relevant spectral band.

In Eq. (16), we demonstrated that the angular sensitivity was independent of the spacing between the surfaces. However, with consideration to signal power, increasing this spacing provides 2 benefits. First, from (15), the number of reflections is inversely proportional to D, and so the effect of imperfect reflective surfaces is diminished as the spacing increases. Second, the area available for incident light increases. If we assume a planar waveguide, the total area A available is given as:

$$A = \frac{D}{\tan(\alpha_0)} W \tag{17}$$

where W is the length of the waveguide in the y-direction. With $D = W = 100$ mm and the incident angle $\alpha_0 = 86.91\ deg$, the total area is 524.08 mm^2, comparable in area to a circle with a radius just under 13 mm.

Practical Considerations: Due to the periodic nature of the ray path, there is 2π ambiguity in measurements of the x-position of the light on the detector. Furthermore, if individual measurements are taken without considering the prior position of the light between measurements, ambiguity can exist where the light path transitions from moving in the positive x direction to the negative x direction. The 2π ambiguity can be reduced by increasing the spacing between mirrors.

In the waveguide model, the mirrors are nominally parallel. Errors in this parallelism can be modelled by rotating the model or coordinate system such the errors in the tilts are symmetric to the z-axis.

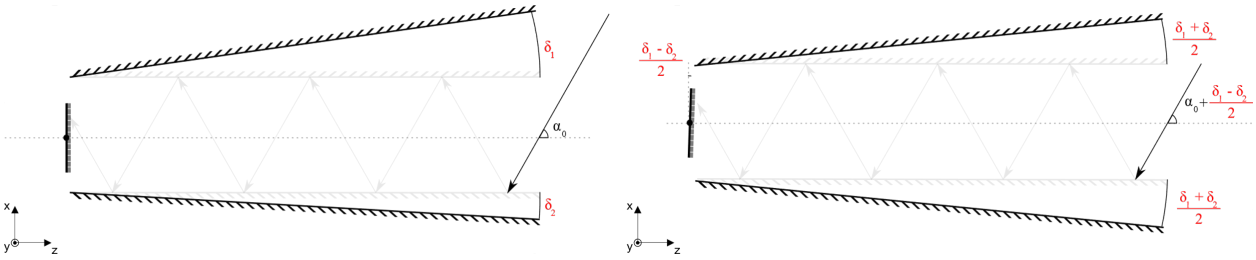

Figure 5. (Left) Arbitrary tilt errors δ_1 and δ_2. (Right) Clock-wise rotation by $(\delta_1$-$\delta_2)/2$ preserves symmetry of the ray-path about the z axis.

Due to tilt angles errors, the waveguide can open towards the incident light (case 1), as seen in Figure 5, or away from it (case 2). In case 1, the tilt angle causes the incident angle α_0 to increase for each reflection while in case 2, the incident angle decreases. In general, after a rotation of the waveguide, the angle α is given as:

$$|\alpha| = |\alpha_0| + (R+1)\left(\frac{\delta_1 - \delta_2}{2}\right) \tag{18}$$

The sign of α is determined by the parity of the number of reflections.

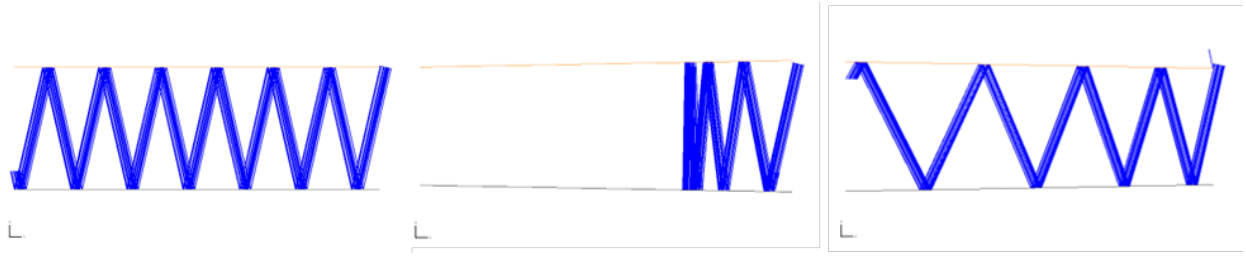

Figure 6. Comparison of ray-path with different tilt errors. (Left) Nominally parallel mirrors; (Middle) Outward tilt of 1 deg in both mirrors (case 1); (Right) Inward tilt in both mirrors (case 2).

Figure 6 illustrates the ray-paths for different tilts. In case 1, due to each reflection, the ray path's angle $|\alpha|$, increases with each reflection. When $|\alpha|$ increases so that its angle is perpendicular to a mirror, the ray deviates out of the waveguide in the opposite direction. If the mirrors' angles are known to a high precision, a waveguide operating in case 2 could be used to further enhance the angular sensitivity for a fixed incident angle of light.

To image the star or stars at the detector, additional optics would be required. One possible method would be to use an echelle grating with a blaze angle of 45 deg on the opposite side to the incident light. Operation of the grating should be in the non-diffraction regime, which would be dependent on period spacing of the grating compared to the wavelength of light. Due to the grating, the ray is reflected, approximately parallel to the waveguide. A lenslet array could then be used to focus to a detector, positioned on the same side as the incident light, facing the waveguide.

2.2.1.3 Metrology for a Two-Star StarNAV Sensor

Methods for measuring and dynamically compensating errors, introduced by the optical components' thermal drift, have been devised. A variant of the heterodyne interferometer presented in reference [27,28] as part of the Space Interferometry Mission Light (SIMS-Lite) [29,30,31], capable of resolving tilt to the microarcsecond level [28], has been incorporated directly into the design of our optical system. A view of this system is depicted in Figure 7 (a) and (b). With reference to Figure 7 (b), light enters the optical system from star 1 and star 2 through mirrors M2 and M3, respectively. These mirrors direct the light into a primary objective lens, which consists of a parabolic mirror, that images the light onto a CCD camera. A fold mirror (M1) ensures that the CCD can be mounted into the same mechanical structure as the objective. A fiber laser is used for internal metrology by injecting light through one of two acousto-optic modulators (AOMs). Both AOM1 and AOM2 are tuned to temporal frequencies f1 and f2, respectively (e.g., 40 MHz and 40.1 MHz [27]). This light is coupled into the system through a 2x2 fiber optic cable array embedded within the parabolic mirror. Light from each fiber is then expanded and collimated through the optical system using the same objective lens and fold mirror M1. Each mirror M2 and M3 has its own identical metrology system. With reference to M2's configuration only (for clarity) per Figure 7 (a), a measurement beam (MB), with frequency f2, is directed towards a 3-element retroreflector array embedded in mirror M2 (or, alternatively, the wedge these are mounted on can be polished to form a mirror). Light reflected from these retroreflectors is then combined with a reference beam (RB), with frequency f1, through two beamsplitters (BS). Each beam is measured with its own high speed single element detector, which are coupled to electronic amplifiers and frequency filters before undergoing phase detection relative to an internally generated electronic reference signal [27]. The phase between each beam can be used to calculate the mirror's tilt, which

can be compensated by actuating the piezotransducers (PZTs) mounted to the mirrors' backside [31]. Our future work will focus on quantifying the sensitivity to misalignment error in the metrology system in order to estimate the impact that the dynamic compensation strategy has on the error budget.

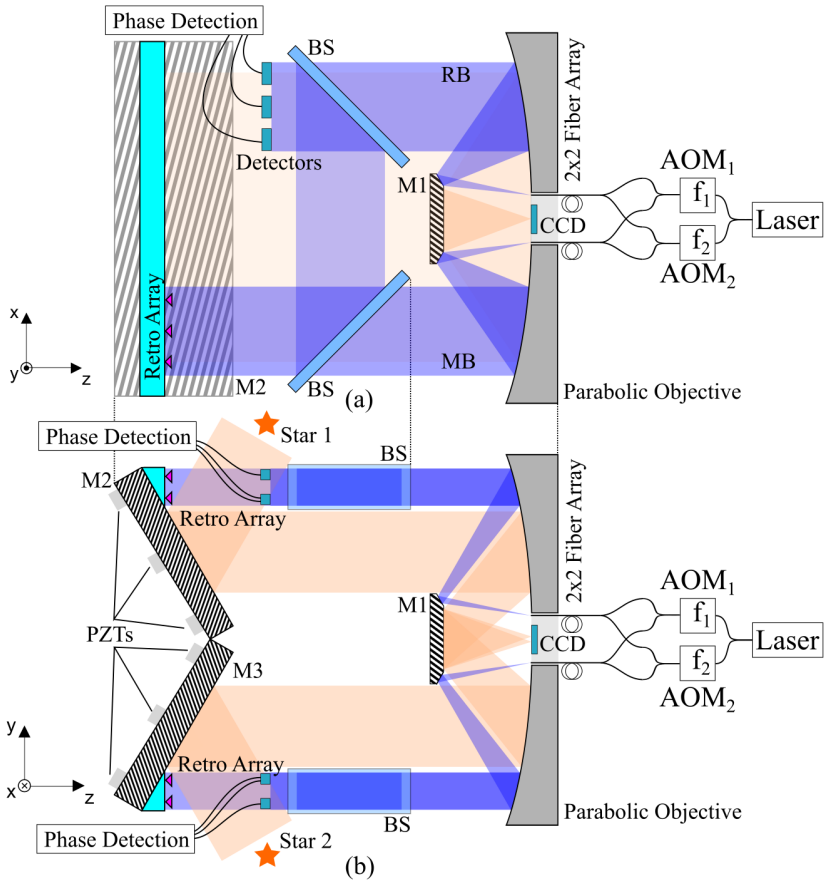

Figure 7. (a) Top-down view illustrating the metrology configuration. (b) Side view (star measurement plane) depicting how the two optical paths are merged onto the same CCD camera.

2.2.2 Wide FOV StarNAV Sensor

Portions of this section also appear in Ref. [32], which was completed with funding from this NIAC Phase I grant.

2.2.2.1 Processing Large Numbers of Star Observations

When considering a wide FOV StarNAV sensor, we may simultaneously view a very large number of stars. The number of stars visible increases dramatically with increasing FOV or star magnitude. Results from a parametric study are shown in Figure 8, which indicates that we can easily obtain images with many thousands of stars. Differentiating between such a large number of stars requires adequate spatial resolution and signal-to-noise ratio—considerations which are revisited in the sensor design.

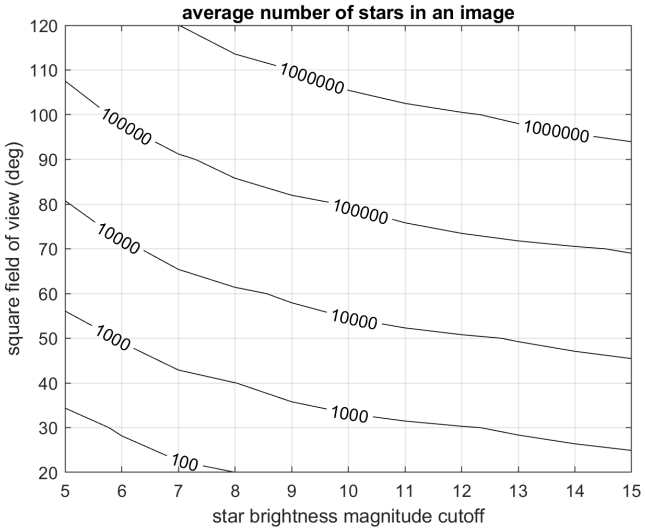

Figure 8. As star brightness magnitude cutoff and FOV increase, the average number of stars in an image increases. In an extreme case, a camera is theoretically capable of capturing over 1 million stars in a single image.

To produce StarNAV measurements without microarcsecond attitude knowledge requires we process inter-star measurements instead of absolute star direction measurements. Initially one might hope to compute the inter-star angle between the largest possible set of independent star pairs (see Figure 9, middle frame)., but solving for the maximum likelihood velocity in such a scenario creates a densely populated measurement covariance matrix. Since there are many millions of star pairs, the computation and use of such a matrix large and fully populated matrix is impossible on a spaceflight computer. Therefore, we instead choose to use each star only once to create uncorrelated StarNAV measurements (see Figure 9, right frame). This, in turn leads to a diagonal covariance matrix, which is inexpensive to compute and trivial to invert.

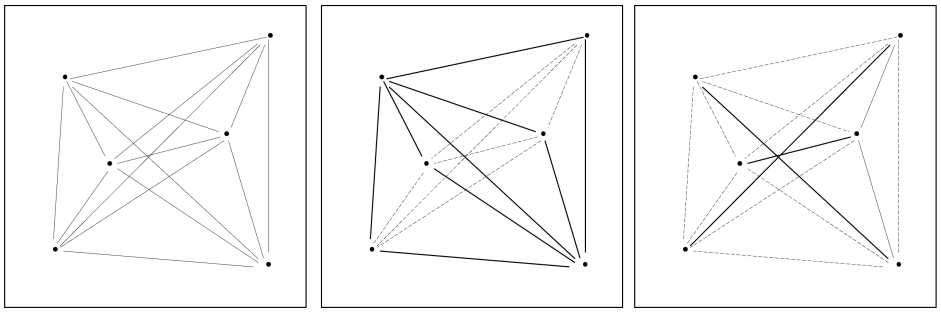

Figure 9. An image containing six stars has 15 possible star pairs (left). Of these, we could choose 9 independent pairs (middle), or we could choose 3 uncorrelated pairs (right).

Begin by isolating the star closest to the top-left of the image and the star closest to the bottom-right of the image. Use these stars to form the first pair. Assuming a dense distribution of stars, this star pair is guaranteed to have an inter-star angle larger than the square FOV of the camera and is guaranteed to have an inter-star angle bisector pointed roughly along the camera boresight direction (near the center of the image).

Divide the image into 16 sections as shown in Figure 10 (far left), and separate stars into 16 bins according to their pixel coordinates in the image. Pair stars from bin 1 randomly to stars in bin 10. Then pair stars from bin 2 randomly to stars in bin 11, and continue on this way pairing stars according to the bin connections shown in Figure 10 (middle left). Once this is done, all stars in 8 of the original 16 sections will be in pairs. There will be leftover stars in the other 8 sections that must still be processed into pairs.

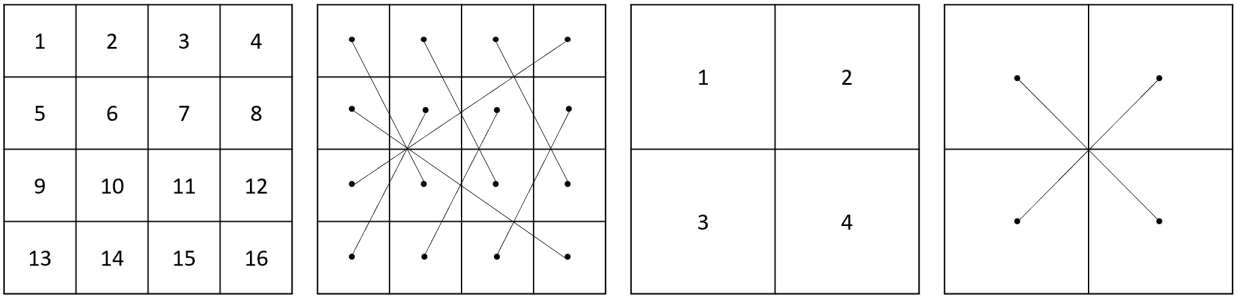

Figure 10. The image is separated into 16 sections (far left) and stars in these sections are paired to stars in other sections (middle left). The remaining stars are separated by their image quadrant location (middle right) and stars are paired between these quadrants (far right).

Next, divide the image into 4 quadrants as shown in Figure 10 (middle right), and separate the unpaired stars into 4 bins according to their pixel coordinates. Pair stars from quadrant 1 randomly to stars in quadrant 4, and pair stars from quadrant 2 randomly to stars in quadrant 3. Once this is done, there will still be unpaired stars in two adjacent quadrants (either 1 and 2, 1 and 3, 2 and 4, or 3 and 4). Pair stars randomly between these two quadrants until only one quadrant has unpaired stars. Finally, pair all remaining stars randomly.

This process is designed to ensure that there few narrow inter-star angles (below 40 degrees) and that inter-star angle bisectors are well-distributed.

2.2.2.2 Parametric Sensor Design

A parametric sweep of sensor design parameters was performed in order to identify a reasonable configuration for a more detailed point design. To achieve this, we let the sensor FOV vary from 30-110 deg and the observed star magnitude vary from 9 to 14. For each point in this space, we consider an optical system with an f-number of F/2 and an aperture sized to yield a signal-to-noise-ratio (SNR) of 15. An SNR of 15 was chosen to provide star centroiding accuracy of at least 0.1 pixel for the majority of the stars. Therefore, at each FOV-magnitude design point we may also compute the image exposure time—with exposures longer that 1 second being considered too long. The result of this analysis is shown in Figure 11, where a black dot indicates the design point for a detailed point study.

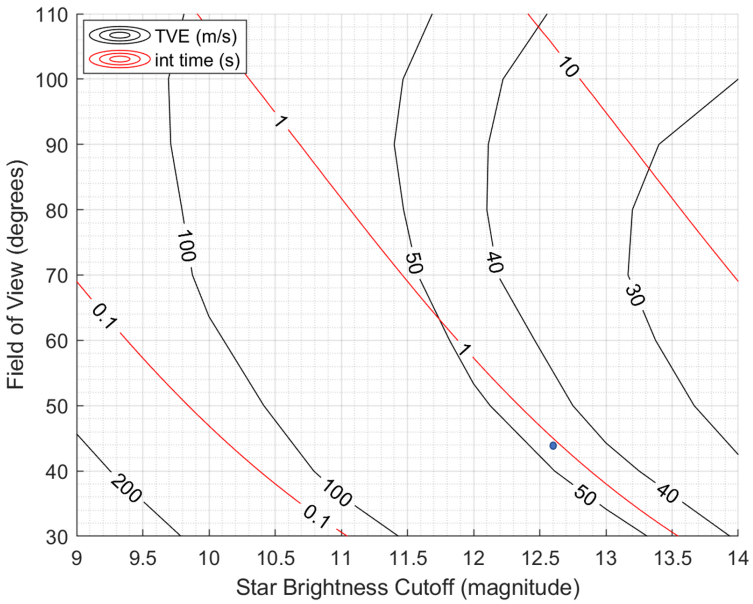

Figure 11. Overlaying contours illustrating the tradespace in integration time (red) and TVE (black). A design point with <1 sec integration time and <50 m/s TVE is shown in the plot. Note: this contour plot uses F/# = 2.

Of note in Figure 11 is that the total velocity error (TVE) does not monotonically decrease with increasing FOV. One might initially expect this to be the case since increasing FOV increases the number of stars—and the error should scale with the inverse square of the number of stars. In this case, however, we have assumed the image is captured by a focal plane of fixed resolution. Thus, increasing the FOV creates a lower instantaneous FOV (iFOV). Moreover, as we view dimmer stars, we begin to find that nearby stars start to cluster together given finite resolution of the detector (see Figure 12). Taking these effects into account produces the performance shown in Figure 11.

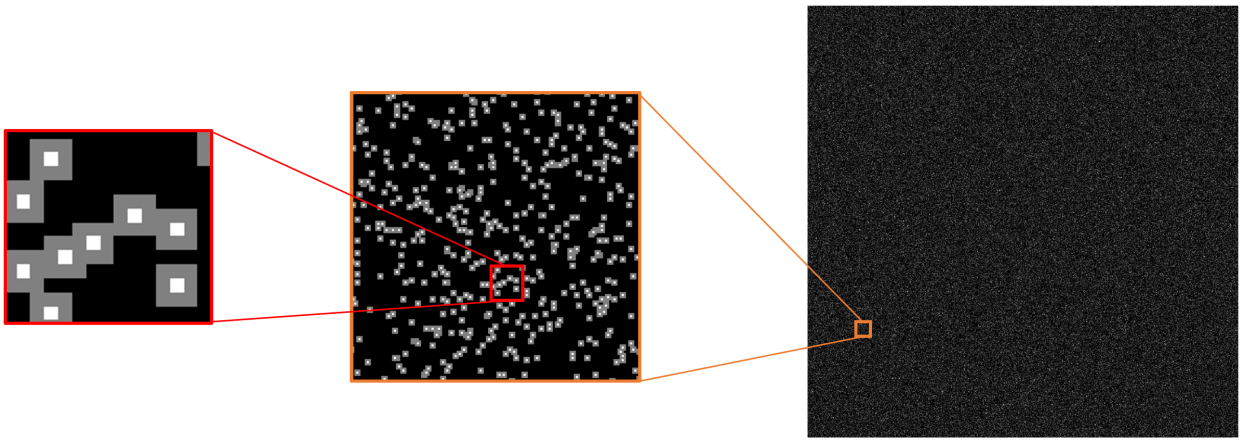

Figure 12. This synthetic star field image consists of 10,000x10,000 pixels, and has over 100,000 stars placed randomly. A close inspection of a small portion of this image highlights the propensity of stars to form clusters in an image.

2.2.2.3 Candidate Sensor Architecture

With a parametric study establishing feasibility, we now consider a specific sensor architecture. The sensor architecture is designed to fit within a 3U CubeSat volume to highlight suitability of this design point for future testing or demonstration. Taking the point design from Figure 11 produces a system with the parameters shown in Table 3.

Table 3. Optical parameters for candidate wide FOV StarNAV sensor.

Optical Design Parameter	Value
Entrance Pupil Diameter	15 mm
F/#	2
FOV	44 deg
Wavelength Range	485-850 nm
Axial Length	249.09 mm

A detailed optical analysis was performed using the Zemax software suite, leading to the lens design shown in Figure 13. The design consists of nine elements, with a single aspheric surface. The three doublets consist of a crown (LAK9G15, $V_D = 54.741$) and flint (SF6G05, $V_D = 25.277$) glass to reduce chromatic aberrations.

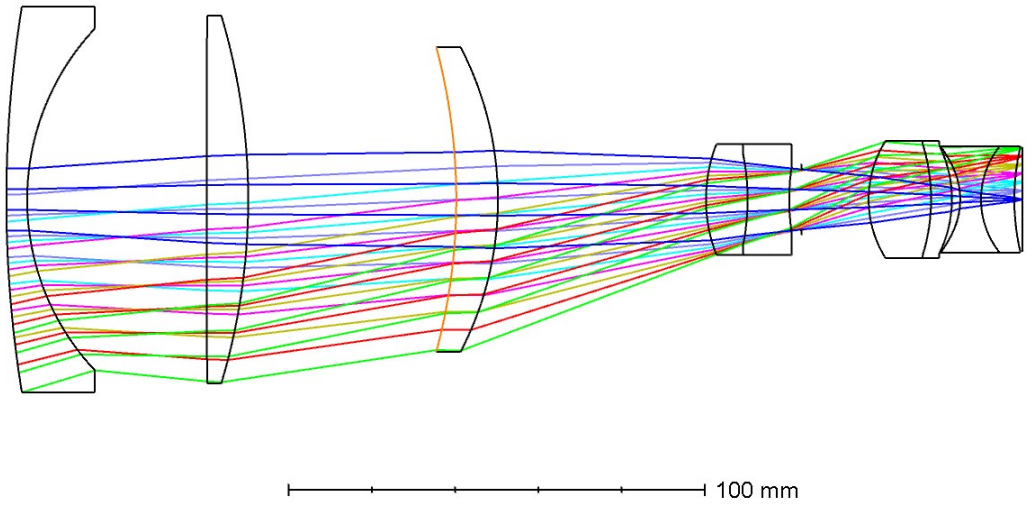

Figure 13. The 2D optical layout is shown with half-field angles of rays between 0 and 22 degrees.

The spot diagram in Figure 14 shows the variation in the spot distribution across different wavelengths and field angles due to geometric aberrations. Nominally, a diffraction-limited performance would minimize centroiding variability. However, the ensquared energy plot (Figure 15), which shows the relative energy in a square region of a given width, demonstrates that greater than 80% of the energy lies within a 7.5 micron half-width for a majority of the wavelength and field ranges. Ideally, a design that maximizes the energy at this half-width point will improve centroiding accuracy.

We also demonstrate that the physical dimensions of the lens design, baffle, and relevant electronics are compatible in a 3U CubeSat (10 cm x 10 cm x 30 cm). This is illustrated by an example of optomechanical design in Figure 16 fit around a 3U chassis model. In the CAD model, we allocate space for 100 MP CCD sensor and electronics, behind and along the side of the furthest lens elements, respectively. The lateral position of the housing (whether it is positioned farthest to the right or left) would be dependent on how a baffle system is deployed (fixed, collapsible, etc.). Beyond this, a stray-light analysis of the optical system would determine a particular baffle design.

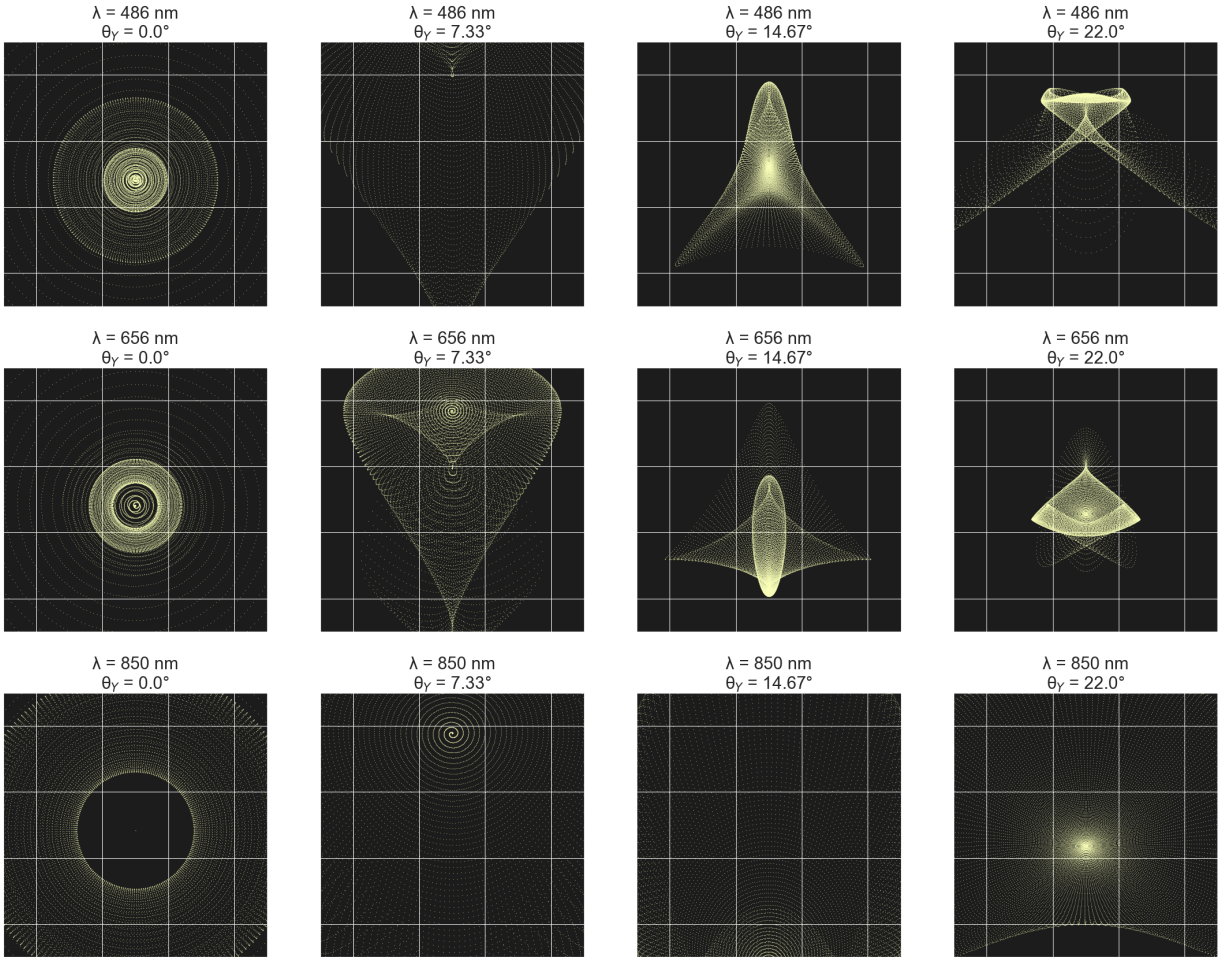

Figure 14. The spot diagrams illustrate the variability in shape and size due to aberrations across fields (θ_Y = 0 to 22 deg) and wavelengths (485 to 850 nm). The grid spacing is 5 μm in both X and Y directions.

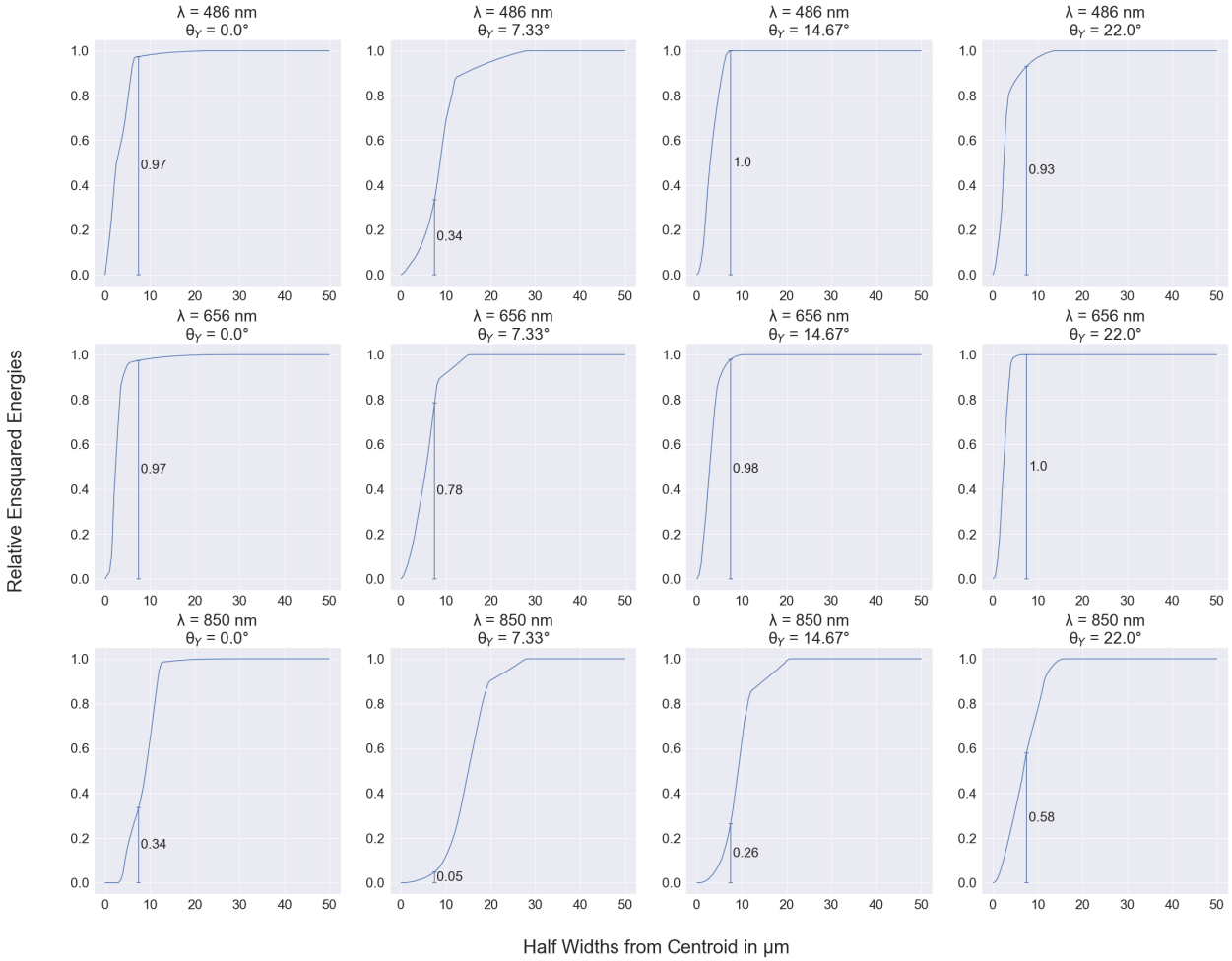

Figure 15. The ensquared energy diagrams show the energy within a square area with a given half width. The vertical lines indicate the amount of energy enclosed in a square with a half-width of 7.5 µm.

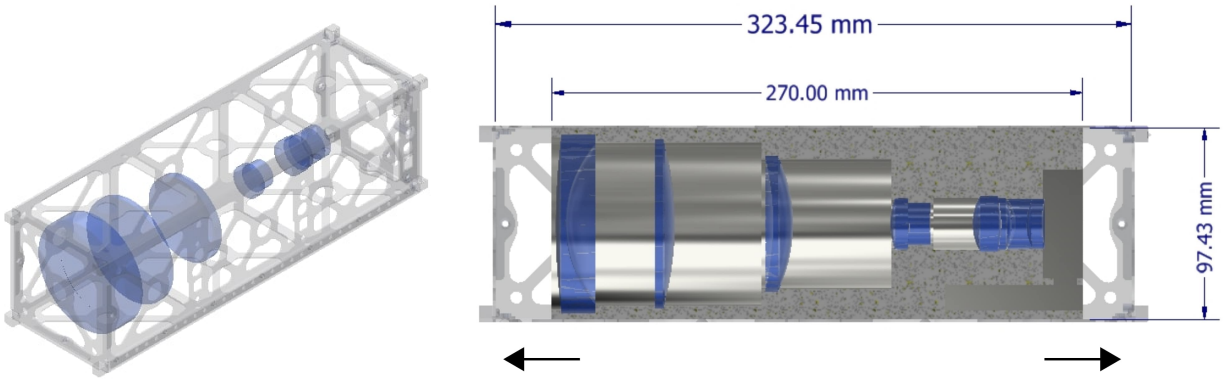

Figure 16. Example of opto-mechanical design within a 3U CubeSat chassis (left). The design can be shifted longitudinally within the chassis, depending on the design of baffle and the electronics layout (right).

2.3 StarNAV for Interstellar Missions

Portions of this section also appear in Ref. [8], which was completed with funding from this NIAC Phase I grant.

Presented here are two case study missions to potential destinations in the interstellar neighborhood around our Solar System. These examples serve to highlight the difficulties in star-based navigation in transit to nearby galactic destinations. Throughout this section we attempt to make minimal assumptions about the profile of the mission or the type of spacecraft making the voyage. These case studies are intended to complement our finding about the non-existence of projective invariants when stars must be modeled as points in three-dimensional space.

2.3.1 Case Study: Mission to Alpha Centauri

Being the closest star system to Earth, the Alpha Centauri system is a logical candidate for the first interstellar mission [33]. Alpha Centauri is a system consisting of three stars: Rigil Kentaurus, Toliman, and Proxima Centauri, also referred to as Alpha Centauri A, B, and C respectively. It is the closest star system to Earth, with Proxima Centauri being the closest individual star at a distance of approximately 4.22 lightyears from the Sun. Two exoplanets have been detected around Proxima Centauri, including an Earth-sized planet in the star's habitable zone [34,35].

Assuming a constant speed of 0.1c, a spacecraft would take just over 42 years to reach Proxima Centauri and another 4.22 years would pass before scientists on Earth begin receiving data sent back via radio signals. The fact that even a mission to the closest star system will require decades of waiting to obtain information highlights the time investment required for interstellar exploration.

Given the close proximity of Alpha Centauri to our Solar System, the pattern of stars on the celestial sphere at Alpha Centauri will appear similar to what we see from Earth. However, while most star directions will be similar, there are a few nearby stars whose apparent direction will change considerably. As an example, consider a spacecraft capable of observing all of the stars in the Hipparcos star catalog. This catalog focuses on bright stars (as seen from Earth), and so includes most of the stars in the interstellar neighborhood around our Solar System. It is possible to calculate the angle by which each star line-of-sight in this catalog is deflected when traveling from Earth to Alpha Centauri (see Figure 17). As one might expect, over 90% of the stars in the catalog that have a positive parallax value are deflected by less than 1 degree. However, dozens of stars are deflected by over 10 degrees. As a comparison, consider instead a spacecraft capable of observing all of the stars in the Gaia star catalog. This catalog focuses on dimmer stars (as seen from Earth) and therefore has many more entries. Taking only the stars brighter than apparent magnitude 15, we find the same trend as before: over 97% of stars that have a positive parallax value deflect by less than 1 degree, but a small number of stars are still deflected by a very large amount (see Figure 17). That a larger percentage of the Gaia catalog (as compared to Hipparcos catalog) has a deflection of less than 1 degree makes sense as Gaia is populated with mostly dim stars—and dimmer stars tend to be further away.

2.3.2 Case Study: Mission to Dorado

Another potential target for interstellar exploration is the TOI-700 system. Located in the Dorado Constellation, TOI-700 is a M-dwarf star at a distance of approximately 101.35 lightyears from the Sun. Three exoplanets have been detected in the system, including TOI-700d, which lies in the habitable zone of the star [36]. TOI-700d is thought to be a super-Earth with a mass between 1.45 and 2.78 times the mass of Earth.

While TOI-700d presents a strong opportunity in the search for life, the significant distance from Earth makes its exploration more challenging than Alpha Centauri. Even a spacecraft traveling at 0.4*c* would take over 253 years to reach the system. Given the time it would take to receive data sent by radio signal back to Earth, information about the stellar system wouldn't be available until 355 years after the spacecraft was launched. Even in a scenario where a spacecraft can be designed to travel at a significant fraction of the speed of light, the number of star systems that can be visited and analyzed in the course of a single human lifetime is very limited.

TOI-700 is almost 25 times further from Earth than Alpha Centauri. As a result, the apparent directions of stars are generally shifted by a much greater amount. Consider again a spacecraft capable of observing all of the stars in the Hipparcos star catalog. For a trip to TOI-700 from Earth, more than half of the stars in the catalog that have a positive parallax value will appear shifted by one degree or more. The median star deflection angle is approximately 6 degrees, and over 30% of stars would be deflected more than 10 degrees (see Figure 17). If the spacecraft instead used the Gaia star catalog, which contains a larger percentage of distant stars, this problem persists. As shown in Figure 17, the median deflection angle for stars brighter than apparent magnitude 15 that have a positive parallax value is between 2 and 3 degrees, and 10% of stars would be deflected more than 10 degrees. These results highlight why it is necessary to treat stars as 3D points for interstellar navigation.

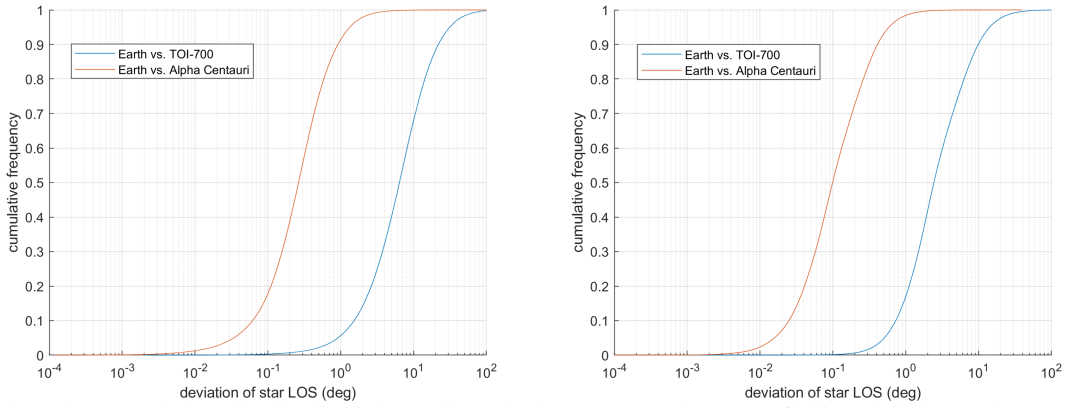

Figure 17. The cumulative distribution of parallax of Hipparcos catalog stars (left) and Gaia catalog stars (right) as seen by an observer at Alpha Centauri (orange) and TOI-700 (blue). Only stars with positive parallax values are considered.

2.3.3 Challenges to Star Identification on Interstellar Missions

The example missions discussed in this section are close to Earth on a galactic scale. The first example, Alpha Centauri, is Earth's closest neighboring star system. The second example is just over 100 lightyears away. Clearly missions to star systems across the galaxy are out of reach. However, even for near-Earth interstellar missions such as those discussed here, we see that a 3D star catalog is needed for navigation. This analysis has made the optimistic assumption that both the Hipparcos and Gaia catalogs have perfect distance knowledge of all stars for which they have usable parallax data. In reality, the uncertainty of distances to stars is often on the order of lightyears. **The effect of parallax means many stars in the Hipparcos and Gaia catalogs will appear so differently in the sky that they would be unrecognizable to star identification algorithms searching in an Earth-based catalog. However, it is important to realize that the very stars that are most robust for star identification purposes are the least helpful for spacecraft position estimation.**

What Figure 17 does not highlight is that the deflection in the apparent line-of-sight to each star will not be in the same direction. Asterisms will change shape relative to their configuration as viewed from Earth. This is well illustrated by considering familiar constellations as viewed from Earth, Alpha Centauri, and TOI-700, as is depicted in Figure 18 to Figure 20. The star patterns include the Big Dipper Asterism from Ursa Major, Orion, and Crux. The constellations appear as translated and misshapen when viewed from a distant observation point. If a spacecraft were to travel to Alpha Centauri, just over 4 lightyears away, these constellations would be measurably different. If a spacecraft were to travel to TOI-700, just over 100 lightyears away, these constellations would be completely unrecognizable. For an observer at TOI-700, the sky would be populated by entirely different constellations, some consisting of the same stars visible from Earth and others consisting of yet undiscovered stars. It is worth noting the extreme parallax in the star γ-Crux as viewed from TOI-700, which required its own sub-plot in Figure 20. The constellation Crux as seen from Earth (gray) and TOI-700 (black) are both shown again in Figure 21 for clarity. The star γ-Crux is 88.5 lightyears from Earth, whereas TOI-700 is over 100 lightyears from Earth, so this star experiences a dramatic parallax shift.

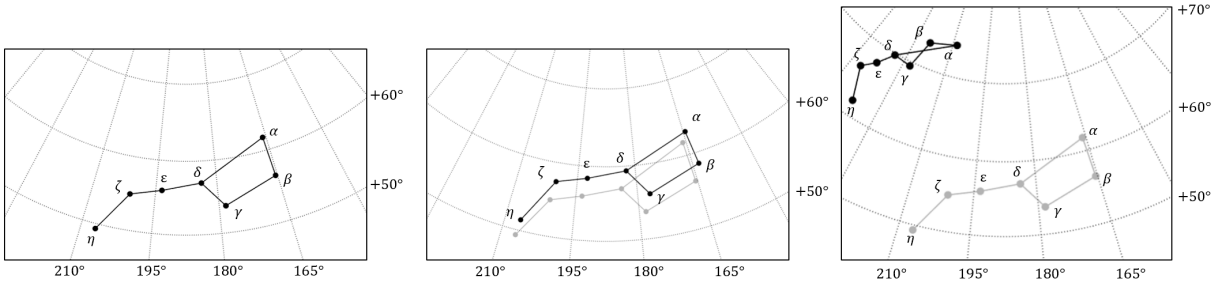

Figure 18. The Big Dipper asterism from the Ursa Major constellation as seen from Earth (left), Alpha Centauri (middle), and TOI-700 (right). The celestial sphere is drawn using a Lambert projection.

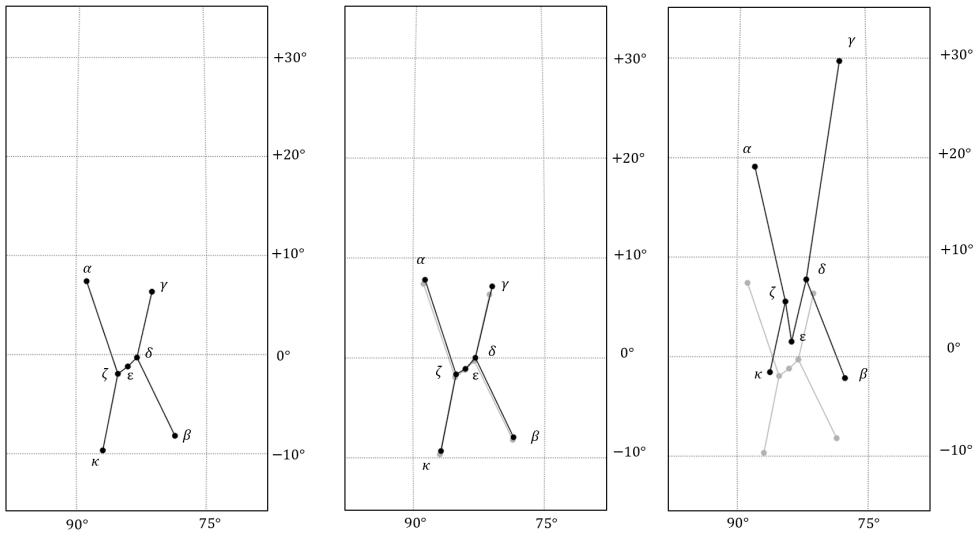

Figure 19. The Orion constellation as seen from Earth (left), Alpha Centauri (middle), and TOI-700 (right). The celestial sphere is drawn using a Robinson projection.

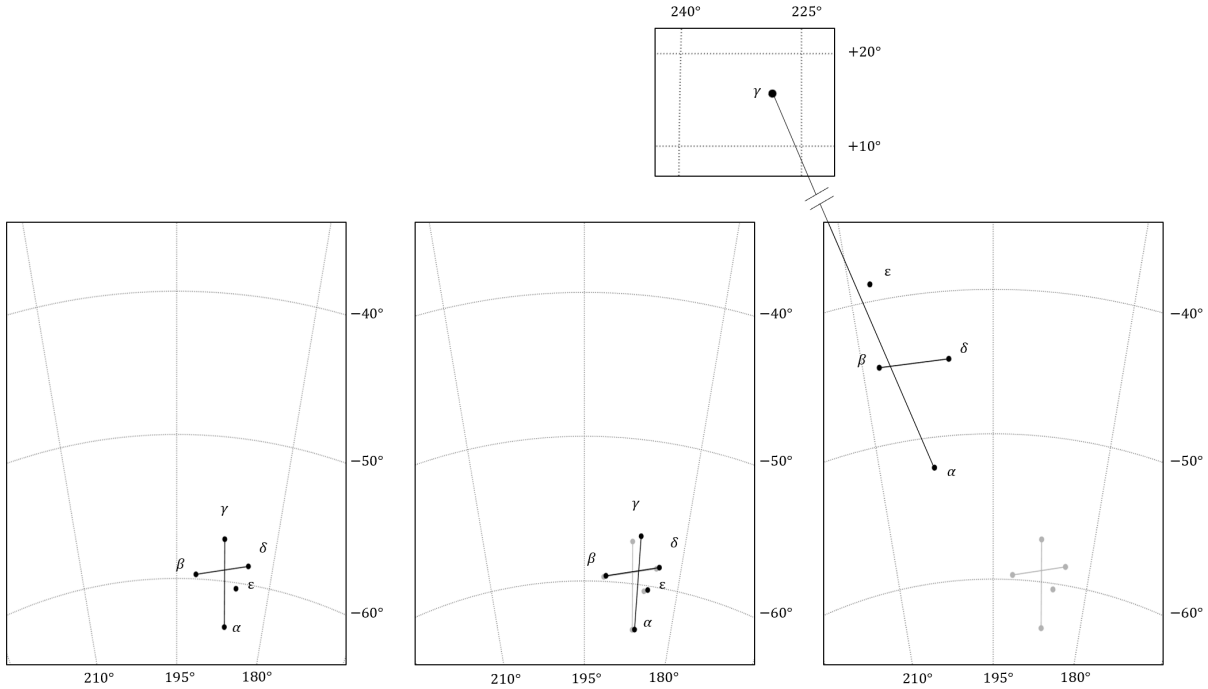

Figure 20. The Crux constellation as seen from Earth (left), Alpha Centauri (middle), and TOI-700 (right). The celestial sphere is drawn using a Lambert projection.

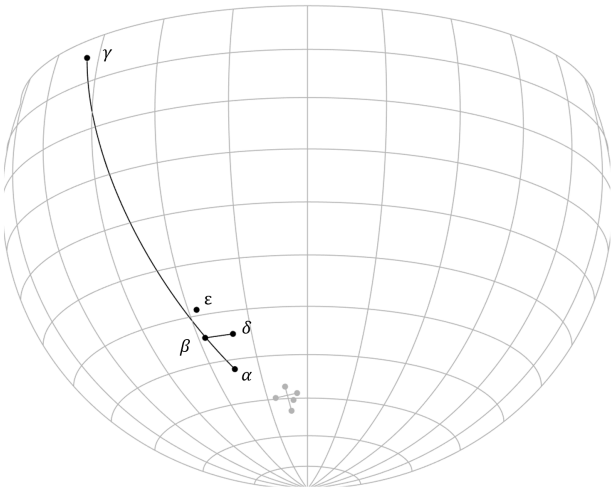

Figure 21. The extreme parallax of gamma-Crux as seen by an observer at TOI-700 (black) as opposed to an observer at Earth (gray). The celestial sphere is drawn using an orthographic projection.

Even for a mission to Alpha Centauri, an Earth-based star catalog will be insufficient for star identification due to the effects of parallax. If one knows their destination star it is possible to separate the star catalog into those stars distant enough for parallax to not noticeably affect their apparent direction, and those stars close enough as to experience dramatic parallax shift. One could then use this distant star catalog for star identification, but another problem arises. The stars that are most useful for star identification, which are farther away and largely immune to parallax, are the least useful for spacecraft position estimation. The opposite problem is also true. Stars close enough to vary in observed line-of-sight substantially with parallax must be treated as 3D points in space, and no general-case view invariants exist to help identify them. A partial remedy is to constrain the spacecraft motion (e.g., a line), but additional work is necessary to identify the best solution to this problem.

3 Summary of Publications

A number of conference and journal publications were written under the support of this NIAC Phase I award. A summary of these publications is as follows:

- Nguyen, H., Kudenov, M.W., and Christian, J.A., "Remarks on the Feasibility of Obtaining StarNAV Measurements within the Solar System," Paper AAS 20-772, *AAS/AIAA Astrodynamics Specialist Conference*, August 2020.
- Christian, J.A., and Crassidis, J.L., "Star Identification and Attitude Determination with Projective Cameras," *IEEE Access*, Vol. 9, 2021, pp. 25,768-25,794.
- McKee, P., Kowalski, J., and Christian, J.A., "Observations on Star-Based Navigation for an Interstellar Mission," *submitted to Acta Astronautica*.
- McKee, P., Christian, J.A., Nguyen, H., and Kudenov, M.W., "StarNAV with a Wide Field-of-View Optical Sensor," *in preparation for Acta Astronautica*.

4 Future Work

The results of this NIAC Phase I study suggest three directions of forward work.

The first and most promising area of forward work is the detailed development of a wide field-of-view (FOV) StarNAV sensor that fits within a CubeSat platform (maturation of the sensor concept shown Section 2.2.2.3). **If found to be feasible after a detailed analysis and complete system design, we believe this to be a strong candidate for a future technology demonstration effort—especially since it fits within a 3U CubeSat volume.** The wide FOV sensor has lower performance than a precision two-star sensor, but it provides a promising alternative for missions with less stringent navigation needs. A technology demonstration using a sensor of this type would provide a good proof-of-concept for the StarNAV idea.

The second area of forward work is continued consideration of high-performance StarNAV with observations of a star pair. As can be seen from Section 2.2.1, such systems tend to be large and complicated—thus making precision two-star configurations undesirable for many practical missions. We remain hopeful that a fundamentally different sensing approach may make these types of measurements feasible, which remain the key to developing a StarNAV system with competitive performance for exploration missions inside the solar system.

The third area of forward work is to consider solutions to the star identification (ID) problem in interstellar space. It has long been assumed that star ID in interstellar space could be achieved in much the same way as within the solar system, with our study being the first to prove this is not the case (which was done by applying well-established theoretical results from another field). Without functioning star ID, it is impossible to perform StarNAV or any other type of star-based navigation.

5 References

1. Christian, J.A., "A Tutorial on Horizon-Based Optical Navigation and Attitude Determination with Space Imaging Systems," *IEEE Access*, Vol. 9, 2021, pp. 19819-19853.
2. Sheikh, S., Pines, D., Ray, P., Wood, K., Lovelette, M., Wolff, M., "Spacecraft Navigation using X-Ray Pulsars," *Journal of Guidance, Control, and Dynamics*, Vol. 29, 2006. pp 49-63.
3. Ely, T., Seubert, J., "One-Way Radiometric Navigation with the Deep Space Atomic Clock," Paper AAS 15-384, *AAS/AIAA Space Flight Mechanics Meeting*, 2015.
4. Christian, J.A., "StarNAV: Autonomous Optical Navigation of a Spacecraft by the Relativistic Perturbation of Starlight," *Sensors*, Vol. 19, No. 19, 2019.
5. Hollenberg, C., Christian, J., "Geometric Solutions for Problems in Velocity-Based Orbit Determination," *The Journal of the Astronautical Sciences*, Vol. 67, 2020, pp 188-224.
6. Norton, R., and Wildey, R., "Fundamental Limitations to Optical Doppler Measurements for Space Navigation," *Proceedings of the* IRE, Vol. 49, 1961, pp. 1655–1659.
7. Shuster, M., "Stellar Aberration and Parallax: A Tutorial," *The Journal of the Astronautical Sciences*, Vol. 51, 2003, pp. 477–494.
8. Christian, J.A., and Crassidis, J.L., "Star Identification and Attitude Determination with Projective Cameras," *IEEE Access*, Vol. 9, 2021, pp. 25,768-25,794.
9. McKee, P., Kowalski, J., and Christian, J.A., "Observations on Star-Based Navigation for an Interstellar Mission," *submitted to Acta Astronautica*.
10. Mundy, J.L., and Zisserman, A., *Geometric Invariance in Computer Vision*, MIT Press, Cambridge, MA, 1992.
11. Zisserman, A., Forsyth, D., Mundy, J., Rothwell, C., Liu, J., and Pillow, N., "3D object recognition using invariance," *Artificial Intelligence*, Vol. 78, pp. 239-288, 1995.
12. Spratling, B., and Mortari, D., "A survey on star identi_cation algorithms," *Algorithms*, Vol. 2, pp. 93-107, 2009.
13. Rijlaarsdam, D., Yous, H., Byrne, J., Oddenino, D., Furano, G., and Moloney, D., "A survey of lost-in-space star identication algorithms since 2009," *Sensors*, Vol. 20, No. 9, #2579, 2020.
14. Derksen, H., and Kemper, G., *Computational Invariant Theory, 2nd Ed.*, Springer, 2015.
15. Gallier, J., *Geometric Methods and Applications, 2nd ed.*, Springer-Verlag, 2011.
16. Christian, J.A., Derksen, H., and Watkins, R.,
17. Burns, J.B., Weiss, R.W., and Riseman, E.M., "The non-existence of general-case view-invariants," in *Geometric Invariance in Computer Vision*, MIT Press, 1992, pp. 120–131.
18. Clemens, D.T., and Jacobs, D.W., "Space and time bounds on indexing 3D models from 2D images," *IEEE Trans. Pattern Analysis Machine Intelligence*, Vol. 13, No. 10, 1991, pp. 1007-1017.
19. Zisserman, A., Forsyth, D., Mundy, J., Rothwell, C., Liu, J., and Pillow, N., "3D object recognition using invariance," *Artificial Intelligence*, Vol. 78, No., 1-2, 1995, pp. 239-288.
20. Hjaltason, G.R., and Samet, H., "Index-driven similarity search in metric spaces (Survey Article)," *ACM Trans. Database Systems*, Vol. 28, No. 4, 2003, pp. 517-580.
21. Mortari, D., Samaan, M.A., Bruccoleri, C., and Junkins, J.L., "The pyramid star identification technique," *Navigation*, Vol. 51, No. 3, 2004, pp. 171-183.

22. Lang, D., Hogg, D.W., Mierle, K., Blanton, M., and Roweis, S., "Astrometry.NET: Blind astrometric calibration of arbitrary astronomical images," *Astronomical Journal*, Vol. 139, No. 5, 2010, pp. 1782-1800.
23. Górski, K.M., Hivon, E., Banday, A.J., Wandelt, B.D., Hansen, F,K, Reinecke, M., and Bartelmann, M., "HEALPix: A framework for high-resolution discretization and fast analysis of data distributed on the sphere," *Astrophysical Journal*, Vol. 622, No. 2, 2005, pp. 759-771.
24. Arnas, D., Fialho, M.A.A., and Mortari, D., "Fast and robust kernel generators for star trackers," *Acta Astronautica*, Vol. 134, 2017 pp. 291-302.
25. Bentley, J.L., and Friedman, J.H., "Data structures for range searching," *ACM Computing Surveys*, Vol. 11, No. 4, 1979, pp. 397-409.
26. Nguyen, H., Kudenov, M.W., and Christian, J.A., "Remarks on the Feasibility of Obtaining StarNAV Measurements within the Solar System," Paper AAS 20-772, *AAS/AIAA Astrodynamics Specialist Conference*, August 2020.
27. Hahn, I., Sandhu, J., Weilert, M., Smythe, R., Nicaise, F., Kang, B., Dekens, F., and Goullioud, R., "Anintroduction to the Guide-2 telescope testbed for the SIM Planet Quest Light mission," *Optical and Infrared Interferometry*, Vol. 7013, Jul 2008.
28. Hahn, I., Weilert, M., Wang, X., and Goullioud, R. "A heterodyne interferometer for angle metrology," *Review of Scientific Instruments*, Vol. 81, Apr 2010.
29. Goullioud, R. and Catanzarite, J.H., "Looking for Earth-like Planets with the SIM Planet Quest LightMission," *2008 IEEE Aerospace Conference*, Mar 2008.
30. Shao, M., and Nemati, B., "Sub-Microarcsecond Astrometry with SIM-Lite: A Testbed-based Performance Assessment," *Publications of the Astronomical Society of the Pacific*, Vol. 121, Jan 2009, p. 41-44.
31. Shields, J.F., Boussalis, D., Fathpour, N., Weilert, M., Hahn, I., and Ahmed, A., "SIM Lite Guide-2telescope system identification, control design and pointing performance evaluation," Optical and Infrared Interferometry II, Vol. 7734, Jul 2010.
32. McKee, P., Christian, J.A., Nguyen, H., and Kudenov, M.W., "StarNAV with a Wide Field-of-View Optical Sensor," *in preparation for Acta Astronautica*.
33. Parkin, K.L.,G., "The breakthrough starshot system model," Acta Astronautica, Vol. 152, 2018, pp. 370–384.
34. Anglada-Escude, G., et al., "Aterrestrial planet candidate in a temperate orbit around proxima centauri," *Nature*, Vol. 536, 2016.
35. Damasso, M., et al., "A low-mass planet candidate orbiting proxima centauri at a distance of 1.5au," *Science Advances*, Vo. 6, 2020.
36. Rodriguez, J.E., et al., The first habitable-zone earth-sized planet from TESS. ii. spitzer confirms toi-700 d, *The Astronomical Journal*, Vol. 160, 2020.